Journal Name

ARTICLE TYPE

Cite this: DOI: 00.0000/xxxxxxxxxx

Stable and high yield growth of GaP and GaAs nanowires arrays using In as a catalyst†

Andrea Scaccabarozzi,[ab] Andrea Cattoni,[a] Gilles Patriarche,[a] Laurent Travers,[a] Stéphane Collin,[a] Jean-Christophe Harmand,[a] Frank Glas[a] and Fabrice Oehler*[a]

Received Date
Accepted Date

DOI: 00.0000/xxxxxxxxxx

We report the first investigation of indium (In) as the vapor-liquid-solid catalyst of GaP and GaAs nanowires by molecular beam epitaxy. A strong asymmetry in the Ga distribution between the liquid and solid phases allows one to obtain pure GaP and $In_{0.2}Ga_{0.8}As$ nanowires while the liquid catalyst remains nearly pure In. This uncommon In catalyst presents several advantages. First, the nanowire morphology can be tuned by changing the In flux alone, independently of the Ga and group V fluxes. Second, the nanowire crystal structure always remains cubic during steady state growth and catalyst crystallization, despite the low contact angle of the liquid droplet measured after growth (95°). Third, the vertical yield of In-catalyzed GaP and (InGa)As nanowires arrays on patterned silicon substrates increases dramatically. Combining straight sidewalls, controllable morphologies and a high vertical yield, In-catalysts provide an alternative to the standard Au or Ga alloys for the bottom-up growth of large scale homogeneous arrays of (InGa)As or GaP nanowires.

1 Introduction

Regular arrays of III-V semiconducting nanowires (NWs) are of great interest for the future generation of opto-electronic devices[1–3]. In the bottom-up approach, the fabrication always includes the use of patterned substrates, fabricated by lithography, to obtain regular arrays of holes in a dielectric mask[4–6] or to localize gold particles[3,7,8]. The type of catalyst, or the absence thereof, is a critical choice which impacts all subsequent steps.

For GaAs and GaP NWs fabricated by molecular beam epitaxy (MBE), growth usually proceeds via the Vapor-Liquid-Solid (VLS) mechanism[9]. Regarding regular Ga(AsP) NW arrays, only two catalysts are reported to provide high yield, stable growth and smooth morphologies: gold (Au-catalyzed)[10,11] or gallium (self-catalyzed)[12–15].

The self-catalyzed variant[16] provides an elegant route to complex multi-shell structures in a single growth run[14] by consuming the Ga VLS catalyst *in situ*[17,18]. However this can lead to crystal phase heterostructures due to the changing contact angle of the Ga catalyst as its volume shrinks[19]. Moreover, as both Au- and Ga-catalysts contain significant amounts of Ga, there is a limit to the sharpness of axial group III heterostructures due to a reservoir effect[20,21]. There is thus an interest to identify new catalysts for the VLS growth of GaAs and GaP NWs which could minimize the reservoir effect, ensure the formation of a single III-V crystal phase during its consumption and retain a high yield of vertical NWs with straight sidewalls.

In this work, we investigate metallic indium (In) as the VLS catalyst of GaAs and GaP NWs. Contrary to Au- and Ga-catalysts, the III-V components consumed in the growth process (Ga, As, P) only sum up here to a minute fraction of the catalyst and the liquid droplet remains mostly In.

To differentiate clearly the chemical composition of the catalyst from that of the solid, we refer to In-catalyzed GaAs NWs as [In]-GaAs, where the term in bracket denotes the main constituent of the liquid droplet. In this notation, self- and Au-catalyzed GaAs NWs are written as [Ga]-GaAs and [Au]-GaAs respectively. Alloying in the solid phase is denoted by parentheses.

Indium has already been used for the self-catalyzed VLS growth of [In]-In(AsSb)[22] or [In]-In(AsP)[23], for which it is a major component of both the solid and liquid phases. However it is the first time that In is reported as a foreign VLS catalyst, akin to gold, for which little to no catalyst material incorporates in the solid phase.

Regarding GaAs-based compounds, our [In]-(InGa)As NWs constitute a novel combination which complements the systems studied so far, such as standard [Au]-(InGa)As NWs[24–26], which growth proceeds from Au-In liquid catalysts, and catalyst-free (InGa)As NWs[27,28], for which no liquid droplet is present during growth[29]. As for GaP, the growth of [Au]-GaP[11] and [Ga]-GaP[15,30] NWs is reported but the case of [In]-GaP NWs has

[a] *Université Paris-Saclay, CNRS, Centre de Nanosciences et de Nanotechnologies, 91120, Palaiseau, France. E-mail: fabrice.oehler@c2n.upsaclay.fr*
[b] *Institut Photovoltaïque d'Ile-de-France, 91120, Palaiseau, France.*

† Electronic Supplementary Information (ESI) available: Equilibrium group V concentration in the droplet for [In]-(InGa)As and [In]-(InGa)P NWs; Thermodynamic reference data; Crystal structure of [Ga]-GaP NWs which catalyst has been crystallized using P. See DOI: 00.0000/00000000.

never been investigated.

2 Solid-liquid distribution

The chemical compositions of the liquid (catalyst) and solid (NW) in the VLS growth of III-V NWs are often very different. The group V is an obvious example: it constitutes 50% of the solid phase but at most a few percent of the liquid[19,31–33]. Group III alloys can also present a severe asymmetry between the solid and liquid phases. For example, the strong distribution asymmetry of (Al,Ga) was used by Priante *et al.* to obtain sharp (AlGa)As heterostructures[21].

The detailed modeling of the VLS growth of NWs from liquid alloy particles has recently been performed using nucleation theory (NT)[25,32,34]. Alternatively, Standard equilibrium thermodynamics (SET) is a simpler method[30]. In Fig. 1, we compare these two methods by plotting the pseudo-binary distribution coefficient of a solid $In_{1-x}Ga_xP$ NW in contact with an [InGaP] liquid catalyst (black curves). The curves relate the GaP composition x in the solid to the Ga fraction y in the liquid at a given temperature T. Similar curves are presented for $In_{1-x}Ga_xAs$ solid NWs in contact with an [InGaAs] liquid droplet (blue curves).

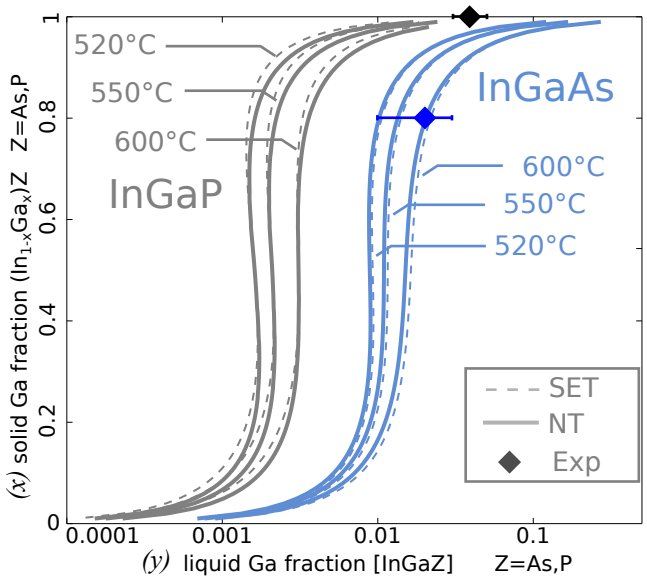

Fig. 1 Distribution coefficient of [InGaP] (black) and [InGaAs] (blue) liquids respectively in contact with pseudo-binary $In_{1-x}Ga_xP$ and $In_{1-x}Ga_xAs$ solids at three different temperatures. Nucleation theory (NT) is compared with standard equilibrium (SET) and experimental data (Exp) at 520°C from this work.

The solid curves (NT) are plotted from equations (29) and (30) of ref[32], assuming a small group V concentration in the droplet ($c_V \ll 1$). The dashed curves (SET) are computed using standard equilibrium equations. All relevant thermodynamical data and methods are summarized in the Supplementary Information†. Our pseudo-binary distribution coefficients are consistent with those of older literature, which are limited to higher temperatures[35].

We note that the SET and NT curves nearly coincide over all the explored composition range. This typical of NW growth and was already observed by Glas on [Ga]-(AlGa)As NWs[34]. It relates to the low concentration of group V in the liquid catalyst, as computed using SET (see Supplementary Information†) or deduced from other experiments[36].

From both NT and SET, we find that the Ga distribution is strongly asymmetric. This particular Ga distribution is not unique to our system and similar curves were calculated for ternary [Au]-(InGa)As NWs using NT[25]. These fast changes in the solid (x) at near constant liquid composition (y) are often hindering the fabrication of NW with uniform composition. Yet, away from these abrupt changes, the solid composition varies slowly over large ranges of liquid composition. Most relevant to the present work, Ga contents (x) in solid $In_{1-x}Ga_xP$ and $In_{1-x}Ga_xAs$ reach near unity while the Ga fractions (y) in the liquid remain below a few atomic percents. Hence the VLS growth of nearly pure GaP and GaAs NWs from nearly pure In catalyst seems achievable.

3 Steady state growth

In light of the above calculations, we have proceeded to grow [In]-(InGa)P and [In]-(InGa)As NWs on patterned Si(111) substrates using MBE (see experimental). Both In and Ga atoms are supplied continuously to sustain the NW growth so that In evaporation is compensated and the catalyst composition remains In-rich. Compared to [Ga]-GaAs or [Ga]-GaP NWs, typically grown at 600°C[15,36], the substrate temperature is reduced to 520°C to limit the evaporation of In adatoms. Identical Si(111) wafers with hexagonal arrays (300 nm pitch) of 50 nm diameter holes in a 14 nm thick silica mask are used to grow selectively the GaAs and GaP NWs. The details of the growth and patterning procedures can be found in the experimental section.

Figures 2.a and 2.b present overviews of [In]-(InGa)P and [In]-(InGa)As NW arrays observed by scanning electron microscopy (SEM). The In-catalyzed NWs grow perpendicularly to the Si(111) surface, similarly to standard Au- and Ga-catalysed GaAs and GaP NWs. This suggests that the NW growth direction remains along the [111] axis despite the unusual In-rich catalysts. This is later confirmed by transmission electron microscopy (TEM). To quantify the composition along the wire, energy dispersive X-ray spectroscopy coupled to scanning transmission electron microscopy (STEM-EDS) is performed on individual NWs. Figures 2.c and 2.d present chemical maps and High Angle Annular Dark Field (HAADF) images (inserts) of In-catalyzed GaP and GaAs NWs. Extracted group III axial composition profiles are shown in Fig. 2.e.

We confirm that the VLS catalyst is essentially In, while the other elements (Ga, As, P) remain near or below the detection limit of the EDS technique. For (InGa)P, we measure $y_{Ga} = 0.02 \pm 0.01$ in the catalyst, while $x_{GaP} = 1.00 \pm 0.01$ in the NW.

For (InGa)As, the solid composition varies slightly along the length of the wire. As the composition of the catalyst could evolve over the duration of growth, we only compare the Ga content in the catalyst $y_{Ga} = 0.01 \pm 0.01$ to the nearest measurement point in the solid $x_{GaAs} = 0.80 \pm 0.02$.

The measurement of Fig. 2 are all performed after growth, at room temperature. Between the growth temperature (520°C)

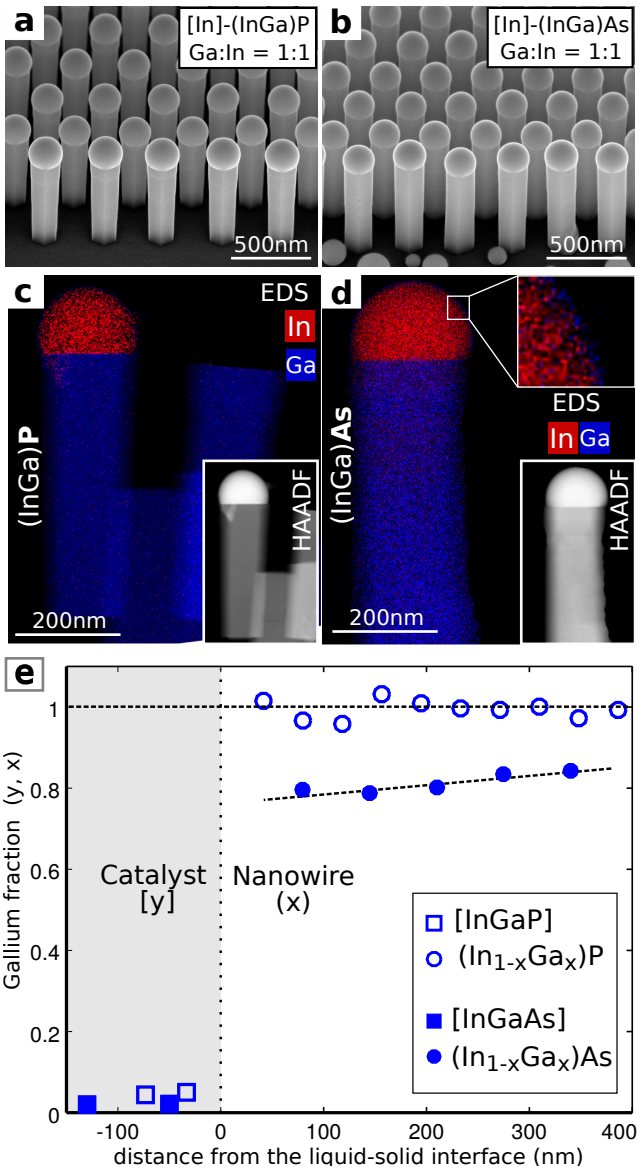

Fig. 2 (a-b) SEM overviews of the [In]-(InGa)P and [In]-(InGa)As NW arrays grown using a Ga:In flux ratio of 1:1. (c-d) STEM-HAADF images and EDS maps of the above NWs dispersed on TEM grids. (e) Gallium composition profiles along the growth axis extracted from the EDS maps. Dotted lines are guides to the eye. Absolute errors are ± 0.01 in the Ga composition and a few nm in length, respectively.

and the STEM experiment, the [InGa] catalyst changes from an homogeneous liquid to a nearly pure In core surrounded by a Ga-rich shell, as expected from the Ga-In binary phase diagram[37]. This Ga-rich shell is seen all around the In catalyst and appears as a thin blue layer (Fig. 2,d top insert). The shell is too thin for composition analysis in our maps, but its highest expected Ga content is the Ga-In eutectic (79% at. Ga)[37]. Our EDX measurements account for this core-shell structure and give its average composition, and therefore the Ga fraction in the homogeneous [InGa] liquid at growth temperature. The measured Ga fraction is close to the detection limit of our system.

These experimental values are reported in Fig. 1 and are in reasonable agreement with the theoretical SET and NT values. Since over 20% of InAs content can be incorporated in the (InGa)As solid phase, we maintain the [In]-(InGa)As notation for arsenide NWs, but we simply refer to phosphide NWs as [In]-GaP, as those contain very little In in the solid.

As regards the initial claim, [In]-GaP NWs are obtained directly but more work would be required to grow pure [In]-GaAs NWs. Thermodynamics suggest that small changes in the In:Ga flux ratio or substrate temperature could lead to a nearly pure GaAs solid (Fig. 1). Still, we already obtain a sound proof of concept, which can showcase the many advantages of In as VLS catalyst.

4 Aspect ratio and morphology

Although there is no significant change of the solid composition when supplying In in our experiments, we observe an obvious evolution of NW morphology. [In]-GaP NWs (Fig. 3,b-c) are wider and shorter than [Ga]-GaP NWs (Fig. 3,a). Table 1 reports average measurements over 10 wires for each sample.

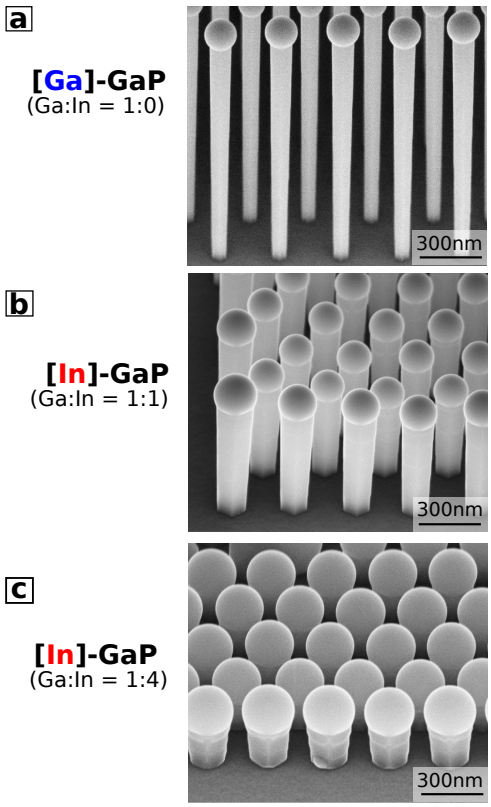

Fig. 3 SEM bird eye view of the NW array (300 nm pitch) after 20 min growth. (a) [Ga]-GaP NWs. (b) [In]-GaP NWs grown using 1:1 (Ga:In) flux ratio. (c) [In]-GaP NWs, 1:4 flux ratio.

To compare quantitatively the NW morphologies, we use the aspect ratio $\mathscr{R}$, computed by dividing the NW height H by the average diameter $(d_{bottom} + d_{top})/2$. The NW volume $\mathscr{V}$ is approximated to a truncated cone. We first observe that $\mathscr{V}$ remains constant with the additional In flux (Ga:In, 1:0 $\mapsto$1:1), despite a change of $\mathscr{R}$ by more than a factor 3. An extra additional In flux (Ga:In, 1:1 $\mapsto$1:4) leads to another drop of $\mathscr{R}$ by a factor 3 and of $\mathscr{V}$ by about 30%.

Ga:In	1:0	1:1	1:4
H (nm)	1055 ± 10	461 ± 10	172 ± 5
d_{bottom} (nm)	78 ± 4	129 ± 5	179 ± 11
d_{top} (nm)	110 ± 5	162 ± 5	219 ± 12
$\mathscr{V}$ (nm^3)	7.4×10^6	7.6×10^6	5.4×10^6
$\mathscr{R}$	11.2	3.1	0.9

Table 1 Measured morphologies of Ga- and In-catalyzed GaP NWs from Fig. 3. The NW height H, the top and bottom diameters d, volume $\mathscr{V}$ and aspect ratio $\mathscr{R}$ are reported.

Since the same Ga and P fluxes are provided to all samples, we can assume that the NW growth remains P-limited, with or without In. Under this assumption, the change of NW morphology at near constant NW volume over a decade of aspect ratio is remarkable. This indicates that the total P capture over the growth duration is almost independent of the NW geometry, including wide variations of radius, height and contact angle. This may be explained by the regular arrayed geometry used in these experiments, which is the same for all samples. If we hypothesize that each wire collects all the available P in its local unit cell[15], we should obtain the same final volume of GaP solid, independently of the very different NW morphologies.

5 Contact angle and crystal phase

Besides the change of NW morphology, the addition of In has a dramatic effect on the VLS liquid catalyst. Figure 4 shows the droplet contact angle β, measured after growth at room temperature using SEM images. The contact angle ($\beta_{In} \simeq 95^\circ \pm 5$, Fig. 4.c) of [In]-GaP NWs grown using a 1:4 flux ratio is much lower than that of [Ga]-GaP NWs ($\beta_{Ga} \simeq 130^\circ$, Fig. 4.a). The NWs grown using 1:4 fluxes shows large irregular side facets (Fig. 4.c), which may affect the contact angle value. However we also estimate a similar contact angle $\beta_{In} \sim 95^\circ \pm 5$ for NWs grown using 1:1 fluxes (Fig. 2.c), which exhibit smoother sidewalls.

Since the liquid is already nearly pure In at the 1:1 flux ratio (Fig. 2.e), its composition does not change significantly when we provide more In (1:1$\mapsto$1:4 fluxes). The constant value of β_{In} thus indicates that the interfacial energies are not affected by the additional In flux. It is thus likely that the NW remains a pure GaP solid, as expected from the thermodynamic analysis (Fig. 1). We thus anticipate a value $\beta_{In} \sim 95^\circ \pm 5$ for all [In]-GaP NWs, provided the In flux is sufficient to maintain an In-rich catalyst.

High resolution STEM (HR-STEM, Fig. 4.b,d) shows that the GaP NWs adopt a twinned cubic zinc blende (ZB) structure, independently of the group III flux ratio, and diffraction contrast TEM (Fig. 5.a) reveals that twinning affects the whole NW length. However, beside the large density of twin boundaries, we do not observe any extended segment of hexagonal wurtzite (WZ). Given the large range of contact angle explored, one might however have expected the NWs to adopt different crystal structures. Recall that, over the 95-130° range, [Ga]-GaAs NWs undergo a double transition ZB$\rightarrow$WZ$\rightarrow$ZB[38] and that a recent calculation predicts [Ga]-GaP NWs to be of WZ structure for $95^\circ < \beta < 105^\circ$. Current models[39,40], confirmed by recent experiments[41], indeed indicate that WZ can form instead of the thermodynamically

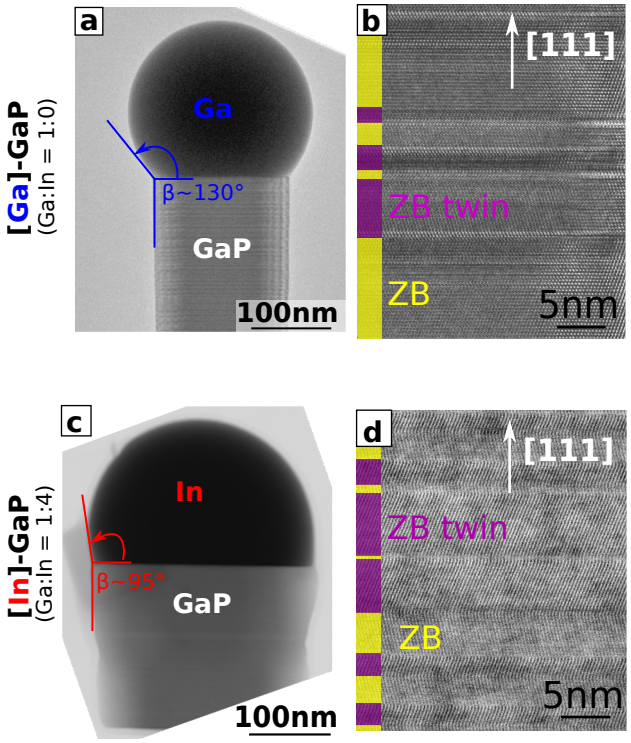

Fig. 4 (a) Bright field TEM image of the catalyst of a [Ga]-GaP NW showing the contact angle β_{Ga}, measured after growth. (b) HR-STEM bright field image showing the crystal structure of the same [Ga]-GaP NW. (c-d) Similar images for the contact angle β_{In} and crystal structure of a [In]-GaP NW grown using 1:4 flux ratio. Cubic phase segments (ZB, yellow color), alternate with twinned cubic segments (ZB twin, purple).

favored ZB provided nucleation occurs at the triple phase line (TPL), which is most likely to occur at intermediate contact angles[39,40]. However, the surface tension of liquid In (0.528 J.m^{-2} at 520°C) is lower than that of liquid Ga (0.676 J.m^{-2})[25] and this makes TPL nucleation less favorable[39]. This may explain the absence of WZ, even at contact angles not far from 90°.

An alternative explanation is that the post-growth contact angle β_{In} does not correspond to the actual configuration during growth. More precisely, the value of β_{In} measured after growth may be much smaller than the actual contact angle during growth, due to the high evaporation rate of In at the growth temperature (see experimental).

6 Catalyst consumption

To circumvent the possible difference of contact angles during and after growth, we have explored a large range of contact angles during growth by proceeding to the catalyst consumption of [In]- and [Ga]-GaP NWs.

Instead of feeding additional In to enlarge the NW catalyst (Fig. 3), we can stop the In flux and let In evaporate from the droplet. If the Ga flux is also stopped while maintaining the group V flow, it is also possible to consume the Ga fraction of the liquid catalyst, effectively eliminating the whole liquid catalyst from the top of the NW.

Figure 5 presents an [In]-GaP NW, which catalyst has been

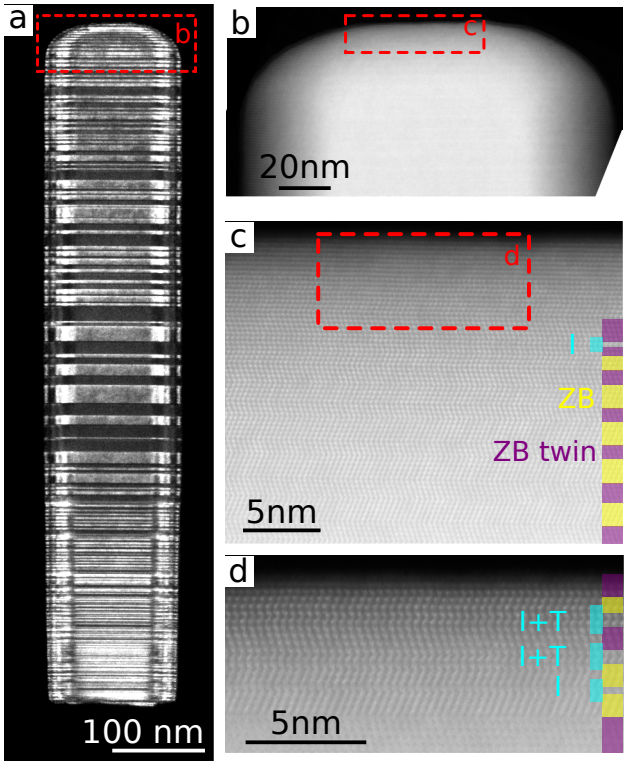

Fig. 5 TEM analysis of [In]-GaP NWs grown using 1:1 (Ga:In) flux ratio which catalyst has been consumed using a P flux. (a) Dark field TEM (111) image which contrast highlights the local cubic twin orientation. The dotted rectangle marks the position of the zone detailed in b. (b-d) HR-STEM images near the top of the NW, closing progressively to the final atomic layers. The ZB phase (yellow) and ZB twin (purple) are indicated, in addition to WZ insertions (cyan) as intrinsic staking faults (I) or twinning combined to stacking fault (I+T).

consumed by supplying P during 20 min. The top of the NW (Fig 5.a-b) is rounded, which indicates that the small fraction of Ga material in the catalyst crystallizes as GaP while the droplet is shrinking.

Figure 5.b-d shows HR-STEM images, closing progressively to the top of the NW. Far from the top (Fig. 5.c), the twinned cubic structure is observed, similar to that of the main NW section (Fig. 5.a). Each cubic twinned segment (ABC↦BAC) is separated by a stacking fault defect (AB**C**BAC), which corresponds to 1ML WZ arrangement (marked in bold font). Closer to the surface (Fig. 5.b-c) we observe a few intrinsic stacking faults (I), AB**CB**CAB, which corresponds to 2ML WZ. In the final layers near the top surface (Fig. 5.d), we observe two defects (I+T) which combine intrinsic stacking fault and twin characters, AB**CBC**BAC, equivalent to 3 hexagonal layers. Except from these short hexagonal sequences, from one (twin) to three (I+T) layers, no extended WZ segment forms during the crystallization of the Ga fraction of the In catalyst.

The same experiment performed on [Ga]-GaP NWs yields a radically different structure (see Supplementary Information†), with an extended WZ section sandwiched between ZB segments.

If the contact angles vary significantly between during and after growth, we expect a larger value of β_{In} during steady state growth (i.e over 95°). Through the course of the In catalyst consumption, the contact angle will sweep through all lower values, including the range of β_{In} which corresponds to the post-growth measurements.

The observed absence of WZ during the whole In catalyst consumption (Fig. 5) thus indicates that WZ nucleation in [In]-GaP NWs is unlikely in a wide range of contact angles. This range starts from $\beta_{In} \simeq 95°$ if the post-growth contact angle is close to the actual one during growth. If the post-growth contact angle is smaller than that of steady state growth, the range is even larger. This further supports our claim that In catalysts have the potential to ensure the growth of NW made of a single (cubic) phase.

7 Vertical yield improvement

Besides the overall stabilization of the ZB phase, the addition of In also induces a substantial increase of the vertical yield of NWs grown on patterned SiO_2/Si(111) substrates. Figure 6 presents representative SEM overviews of the NW arrays after growth. No empty holes are found, which indicates that the Si(111) surface is exposed fully in each hole. However, some wires grow in titled directions (i.e. not vertical) or as a irregular crystals extending over the mask. The average fraction of vertical NWs, i.e. the vertical yield (χ), is summarized in Table 2. We find that [Ga]-GaAs NWs have the lowest yield, which substantially improves as In is provided ([In]-(InGa)As). Arrays of [Ga]-GaP NWs start with a higher vertical yield but also improve slightly when In is supplied ([In]-GaP).

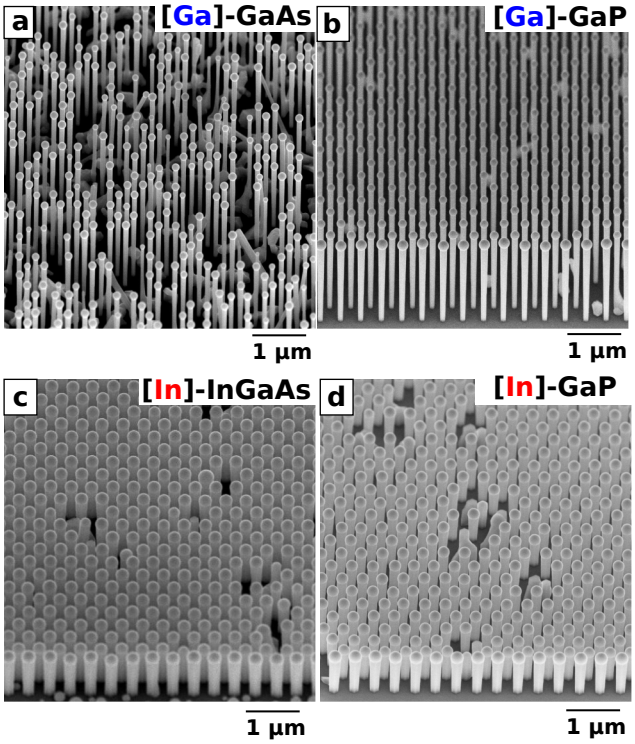

Fig. 6 SEM overviews of NWs arrays on patterned Si(111). (a,b) [Ga]-GaAs and [Ga]-GaP NWs. (c,d) [In]-(InGa)As and [In]-GaP, grown using 1:1 ratio of Ga:In fluxes.

To understand the vertical yield improvement related to In, we have performed short growth experiments (150 s) of (InGa)As

	Ga-catalyzed (1:0)	In-catalyzed (1:1)
(In)GaAs	0.5 ± 0.2	0.8±0.1
GaP	0.8 ± 0.1	0.9±0.1

Table 2 Fraction of vertical NWs in the array (χ), depending on the material and catalyst type (Ga:In flux ratio), averaged over 200 structures.

NWs, as they exhibit the largest yield increase with In. Different Ga:In fluxes (1:0, 2:0, 1:1) were used to investigate the effect of the pre-deposited droplet volume and composition. The (2:0) fluxes obviously provides pure Ga droplets, with a volume similar to that of the [InGa] droplets deposited with the (1:1) fluxes. This allows us to separate the effect of volume increase from that of droplet composition. All other experimental parameters are maintained identical.

Figure 7 presents the SEM images after the droplet deposition step and after 150 s of subsequent NW growth. A single droplet is present in each hole, for all samples and group III fluxes. The droplets grown using the largest group III fluxes (2:0 Fig. 7.b and 1:1 Fig. 7.c) are bigger than those from the (1:0) experiment (Fig. 7.a). After 150 s of growth, the vertical yield difference is already visible. Fig 7.c confirms the yield improvement in the presence of In, as previously observed during the longer growth experiments (Fig. 6). Since the (2:0) flux with large pure Ga droplets also results in a poor vertical yield (Fig. 7.b), this demonstrates that the improved vertical yield is not due to the increased volume of the initial droplet[13], but relates to the presence of In in the liquid catalyst.

The fraction of vertical NWs is known to depend on the droplet contact angle[42,43], hole diameter and mask thickness[44], as well as droplet size[12,13]. In our case, the ratio of hole diameter over mask thickness is about 3.5, which is slightly below the reported optimum range[44]. This may explain the relatively poor vertical yield in our [Ga]-GaAs NW arrays ($\chi = 0.5$). As seen previously, the transition from Ga- to In-catalyst is associated with a strong reduction of the contact angle (from $\beta_{Ga} = 130°$ to $\beta_{In} = 95°$, measured after growth). An optimum value of 90° is reported in the literature for Ga[42,43]. This could explain the vertical yield improvement with In-catalyst observed both in our GaP and GaAs NW arrays.

On the other hand, the vertical yield enhancement from GaAs to GaP NW arrays remains unexplained, as both start from the same droplets arrays and have the same contact angle.

8 Conclusion

We have proposed and demonstrated the VLS growth of GaAs and GaP NWs catalyzed by In droplets, exploiting the strong asymmetry in the distribution of Ga between the liquid and solid phases. Pure GaP and $In_{1-x}Ga_xAs$ ($x \simeq 0.8$) NWs were grown using MBE at 520°C, with nearly pure In liquid catalysts. These offer many growth opportunities, such as the *in situ* tuning of catalyst droplet size and NW aspect ratio over a decade by adjusting the In and Ga fluxes. Due to the low surface energy of In, the crystal structure of the In-catalyzed GaP and (In)GaAs NWs is cubic, despite the low contact angle ($\beta_{In} \simeq 95°$, measured after growth), and remains so even during the complete catalyst crystallization. Finally, this low contact angle is the probable origin of the stark improvement in the vertical NW yield observed for In-catalyzed (InGa)As and GaP NW arrays on patterned Si(111).

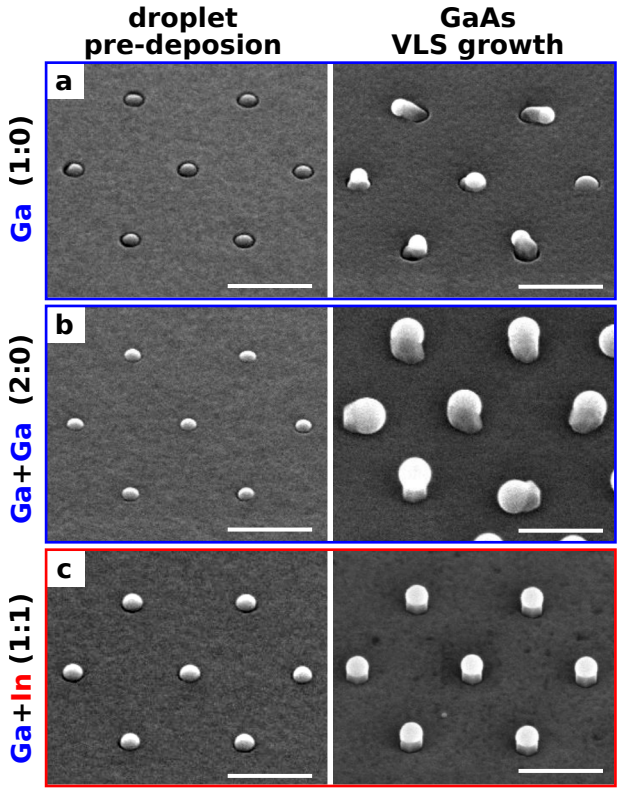

Fig. 7 SEM observations of Ga- and In-catalyzed GaAs NW arrays grown using different Ga:In flux ratio, after the droplet deposition (left) and 150 s of subsequent growth (right). (a) Reference Ga-catalyzed sample, ratio 1:0. (b) Ga-catalyzed sample grown using twice the Ga flux, ratio 2:0. (c) Sample growth using simultaneous In and Ga fluxes, ratio 1:1. Scalebar is 200 nm for all images.

Combining good morphology, stable crystal structure, high vertical yield, as well as *in situ* catalyst crystallization, In provides an interesting alternative to Au- or Ga-catalysts for the bottom-up growth of large scale NW arrays. More work is required to obtain a totally In-free solid in the case of In-catalyzed GaAs NWs, as well as a twin-free crystal structure. However the first controllable growth of In-catalyzed and yet pure GaP NW arrays is fully demonstrated.

Conflicts of interest

There are no conflicts to declare.

Acknowledgements

This project has been supported by the French government in the framework of the "Programme d'Investissement d'Avenir" - ANR-IEED-002-01 and by the ANR projects Nanocell (ANR-15-CE05-0026) and Hetonan (ANR-15-CE05-0009). The TEM tool used in this study was funded by the project TEMPOS (ANR-10-EQPX-50).

Experimental

All samples were grown on 2" p-type (111) Si wafers with 0.01-0.02 Ω.cm resistivity, covered with 25±2 nm of SiO_x using plasma-enhanced chemical vapor deposition. The thickness of the oxide layer was measured for every sample by ellipsometry and reflectometry. On each sample, a hexagonal array of disks with 20 nm nominal diameter and 300 nm pitch was written by electron-beam lithography (EBL, Raith EBPG 5000+) in a polymethylmethacrylate (PMMA) resist layer and developed with a solution of methyl-isobutyl-ketone and isopropyl-alcohol. The EBL pattern was transferred into the oxide layer by reactive ion etching, creating a pattern of holes. Organic residues on the samples were cleaned with solvents and an oxygen plasma. A final wet etch step in diluted hydrofluoric acid (HF) was performed immediately before loading the samples in the MBE system to obtain a fully deoxidized Si(111) surface inside the holes. After this, the thickness of the silicon oxide mask is reduced to 14 nm. Before loading into the growth chamber, the samples were outgassed at about 600°C, then further outgassed in situ at 700°C. Scanning electron microscopy (SEM) inspection prior to the growth but after the outgassing steps reveals an average hole diameter of 50 nm.

The growth was performed in a Riber 32 solid-source MBE reactor. Ga-catalyzed NWs were grown at a substrate temperature of 600°C and In-catalyzed NWs at 520°C. The Ga flux (from a standard effusion cell) corresponds to a growth rate of 1.5 Å.s^{-1} for planar (001) GaAs, as determined using Reflection High Energy Electron Diffraction (RHEED). The In flux (standard effusion cell) was calibrated from (001) InAs RHEED measurements. The As_4 flux (Riber VAC500, cracker temperature 600°C) is set to 1.4 As/Ga effective atomic flux ratio from (001) GaAs RHEED. The P_2 flux (Riber KPC, cracker temperature 900°C) is fixed to a 1.2 P:Ga effective atomic flux using growth rate measurements on a (001) GaP surface.

Prior to the exposure to group V, Ga or InGa droplets are deposited for 2 min, which completely fills each hole of our silica mask. The subsequent NW growth duration is 20 min.

The morphological characterizations were performed by SEM (FEI Magellan 400L), while structural analyses were performed by TEM and STEM/HAADF (FEI Titan Themis operated at 200 kV). The NW chemical composition was measured by EDS (Brucker super X) during the STEM observations.

Notes and references

1 R. Chen, T.-T. D. Tran, K. W. Ng, W. S. Ko, L. C. Chuang, F. G. Sedgwick and C. Chang-Hasnain, *Nature Photonics*, 2011, **5**, 170–175.

2 A. C. Scofield, J. N. Shapiro, A. Lin, A. D. Williams, P.-S. Wong, B. L. Liang and D. L. Huffaker, *Nano Letters*, 2011, **11**, 2242–2246.

3 J. Wallentin, N. Anttu, D. Asoli, M. Huffman, I. Aberg, M. H. Magnusson, G. Siefer, P. Fuss-Kailuweit, F. Dimroth, B. Witzigmann, H. Q. Xu, L. Samuelson, K. Deppert and M. T. Borgström, *Science*, 2013, **339**, 1057–1060.

4 J. Noborisaka, J. Motohisa and T. Fukui, *Applied Physics Letters*, 2005, **86**, 213102.

5 K. Tomioka, J. Motohisa, S. Hara, K. Hiruma and T. Fukui, *Nano Letters*, 2010, **10**, 1639–1644.

6 G. Mariani, P.-S. Wong, A. M. Katzenmeyer, F. Léonard, J. Shapiro and D. L. Huffaker, *Nano Letters*, 2011, **11**, 2490–2494.

7 M. T. Borgström, G. Immink, B. Ketelaars, R. Algra and E. P. A. M. Bakkers, *Nature Nanotechnology*, 2007, **2**, 541–544.

8 I. Aberg, G. Vescovi, D. Asoli, U. Naseem, J. P. Gilboy, C. Sundvall, A. Dahlgren, K. E. Svensson, N. Anttu, M. T. Bjork and L. Samuelson, *IEEE Journal of Photovoltaics*, 2016, **6**, 185–190.

9 R. S. Wagner and W. C. Ellis, *Applied Physics Letters*, 1964, **4**, 89–90.

10 Z. H. Wu, X. Y. Mei, D. Kim, M. Blumin and H. E. Ruda, *Applied Physics Letters*, 2002, **81**, 5177–5179.

11 J. P. Boulanger and R. R. LaPierre, *Semiconductor Science and Technology*, 2012, **27**, 035002.

12 S. Plissard, G. Larrieu, X. Wallart and P. Caroff, *Nanotechnology*, 2011, **22**, 275602.

13 A. M. Munshi, D. L. Dheeraj, V. T. Fauske, D. C. Kim, J. Huh, J. F. Reinertsen, L. Ahtapodov, K. D. Lee, B. Heidari, A. T. J. van Helvoort, B. O. Fimland and H. Weman, *Nano Letters*, 2014, **14**, 960–966.

14 E. Dimakis, U. Jahn, M. Ramsteiner, A. Tahraoui, J. Grandal, X. Kong, O. Marquardt, A. Trampert, H. Riechert and L. Geelhaar, *Nano Letters*, 2014, **14**, 2604–2609.

15 F. Oehler, A. Cattoni, A. Scaccabarozzi, G. Patriarche, F. Glas and J.-C. Harmand, *Nano Letters*, 2018, **18**, 701–708.

16 C. Colombo, D. Spirkoska, M. Frimmer, G. Abstreiter and A. Fontcuberta i Morral, *Physical Review B*, 2008, **77**, 155326.

17 M. H. T. Dastjerdi, J. P. Boulanger, P. Kuyanov, M. Aagesen and R. R. LaPierre, *Nanotechnology*, 2016, **27**, 475403.

18 Y. H. Kim, D. W. Park and S. J. Lee, *Applied Physics Letters*, 2012, **100**, 033117.

19 D. Jacobsson, F. Panciera, J. Tersoff, M. C. Reuter, S. Lehmann, S. Hofmann, K. A. Dick and F. M. Ross, *Nature*, 2016, **531**, 317–322.

20 K. A. Dick, J. Bolinsson, B. M. Borg and J. Johansson, *Nano Letters*, 2012, **12**, 3200–3206.

21 G. Priante, F. Glas, G. Patriarche, K. Pantzas, F. Oehler and J.-C. Harmand, *Nano Letters*, 2016, **16**, 1917–1924.

22 H. So, D. Pan, L. Li and J. Zhao, *Nanotechnology*, 2017, **28**, 135704.

23 G. Zhang, C. Rainville, A. Salmon, M. Takiguchi, K. Tateno and H. Gotoh, *ACS Nano*, 2015, **9**, 10580–10589.

24 F. Jabeen, V. Grillo, F. Martelli and S. Rubini, *IEEE Journal of Selected Topics in Quantum Electronics*, 2011, **17**, 794–800.

25 J. Johansson and E. D. Leshchenko, *Journal of Crystal Growth*, 2019, **509**, 118–123.

26 J. Grecenkov, V. G. Dubrovskii, M. Ghasemi and J. Johansson, *Crystal Growth & Design*, 2016, **16**, 4526–4530.

27 S. Hertenberger, S. Funk, K. Vizbaras, A. Yadav, D. Rudolph,

J. Becker, S. Bolte, M. Döblinger, M. Bichler, G. Scarpa, P. Lugli, I. Zardo, J. J. Finley, M.-C. Amann, G. Abstreiter and G. Koblmüller, *Applied Physics Letters*, 2012, **101**, 043116.

28 G. Koblmüller and G. Abstreiter, *physica status solidi - Rapid Research Letters*, 2013, **8**, 11–30.

29 S. Hertenberger, D. Rudolph, S. Bolte, M. Döblinger, M. Bichler, D. Spirkoska, J. J. Finley, G. Abstreiter and G. Koblmüller, *Applied Physics Letters*, 2011, **98**, 123114.

30 G. Priante, G. Patriarche, F. Oehler, F. Glas and J.-C. Harmand, *Nano Letters*, 2015, **15**, 6036–6041.

31 F. Glas, M. R. Ramdani, G. Patriarche and J.-C. Harmand, *Physical Review B*, 2013, **88**, 195304.

32 V. G. Dubrovskii, *Journal of Physics D: Applied Physics*, 2017, **50**, 453001.

33 F. Glas, J.-C. Harmand and G. Patriarche, *Physical Review Letters*, 2010, **104**, 135501.

34 F. Glas, *Crystal Growth & Design*, 2017, **17**, 4785–4794.

35 M. Panish and M. Ilegems, *Progress in Solid State Chemistry*, 1972, **7**, 39–83.

36 M. R. Ramdani, J. C. Harmand, F. Glas, G. Patriarche and L. Travers, *Crystal Growth & Design*, 2012, **13**, 91–96.

37 T. Anderson and I. Ansara, *Journal of Phase Equilibria*, 1991, **12**, 64–72.

38 F. Panciera, Z. Baraissov, G. Patriarche, V. G. Dubrovskii, F. Glas, L. Travers, U. Mirsaidov and J.-C. Harmand, *Nano Letters*, 2020, 1669–1675.

39 F. Glas, J.-C. Harmand and G. Patriarche, *Physical Review Letters*, 2007, **99**, 146101.

40 V. G. Dubrovskii, *Crystal Growth & Design*, 2017, **17**, 2544–2548.

41 J.-C. Harmand, G. Patriarche, F. Glas, F. Panciera, I. Florea, J.-L. Maurice, L. Travers and Y. Ollivier, *Physical Review Letters*, 2018, **121**, 166101.

42 E. Russo-Averchi, J. V. Plestina, G. Tütüncüoglu, F. Matteini, A. D.-M. M. de la Mata, D. Rüffer, H. A. Potts, J. Arbiol, S. Conesa-Boj and A. Fontcuberta i Morral, *Nano Letters*, 2015, **15**, 2869–2874.

43 F. Matteini, G. Tütüncüoglu, D. Mikulik, J. Vukajlovic-Plestina, H. Potts, J.-B. Leran, W. C. Carter and A. Fontcuberta i Morral, *Crystal Growth & Design*, 2016, **16**, 5781–5786.

44 J. Vukajlovic-Plestina, W. Kim, L. Ghisalberti, G. Varnavides, G. Tütüncüoglu, H. Potts, M. Friedl, L. Güniat, W. C. Carter, V. G. Dubrovskii and A. Fontcuberta i Morral, *Nature Communications*, 2019, **10**, 869.